PAPER

Check for updates

Novel 2D-AuSe nanostructures as effective platinum replacement counter electrodes in dye-sensitized solar cells

Esmie Mposa, [ID] [a] Rudo K. Sithole, [ID] [a] Zakhele Ndala,[a] Grace N. Ngubeni,[a] Kalenga P. Mubiayi,[a] Poslet M. Shumbula,[b] Lerato F. E. Machogo-Phao*[ac] and Nosipho Moloto [ID] *[a]

Studies to improve the efficiency of dye-sensitized solar cells (DSSCs) include, but are not limited to, finding alternatives such as 2D layered materials as replacement counter electrodes (CEs) to the commonly used Pt. Herein, we report for the first time, the use of AuSe as a counter electrode for the reduction of triiodide ions (I_3^-) to iodide ions (I^-). The colloidal synthesis of gold selenide nanostructures produced α-AuSe and β-AuSe dominated products as determined by XRD. Electron microscopy showed α-AuSe having belt-like structures while β-AuSe had a plate-like morphology. EDS mapping confirmed the elemental composition and homogeneity of the AuSe CEs. Cyclic voltammetry curves of the AuSe CEs displayed the double set of reduction−oxidation peaks associated with the reactions in the I_3^-/I^- electrolyte and therefore were comparable to the Pt CV curve. The α-AuSe CE showed better electrocatalytic activity with a reduction current of 6.1 mA than that of β-AuSe and Pt CEs, which were 4.2 mA and 4.8 mA, respectively. The peak-to-peak separation (ΔE_{pp}) for the α-AuSe CE was also more favourable with a value of 532 mV over that of the β-AuSe CE of 739 mV however, both values were larger than that of the Pt CE, which was found to be 468 mV. The EIS and Tafel plot data showed that α-AuSe had the best catalytic activity compared to β-AuSe and was comparable to Pt. The DSSC using α-AuSe as a CE had the highest PCE (6.94%) as compared to Pt (4.89%) and β-AuSe (3.47%). The lower efficiency for Pt was attributed to the poorer fill factor. With these novel results, α-AuSe is an excellent candidate to be used as an alternative CE to Pt in DSSCs.

1. Introduction

Dye-sensitized solar cells (DSSCs) have emerged as a powerful photovoltaic technology alternative to conventional silicon solar cells because of their advantages such as low cost, use of environmentally friendly materials, simple fabrication techniques and acceptable photoelectric conversion efficiencies.[1,2] To date, the highest reported efficiency of lab-scale DSSCs is 14.3%, an increase from 7.1–7.9% first reported in 1991.[3–5] A typical DSSC has four main components; a photoanode made of a mesoporous oxide layer (typically, TiO_2) deposited on a transparent conductive glass substrate; a monolayer of dye sensitizer covalently bonded to the surface of the TiO_2, an electrolyte containing redox couple (typically, I^-/I_3^-), and a counter electrode made of a platinum coated conductive glass substrate.[6,7] The

functioning of DSSCs relies on the interconnection of a multi-component system; therefore improving the device efficiency considers a multifaceted approach. Research on the modification of some of the cell components has been explored. This includes alternative synthesis methods for nanostructured semiconductor materials such as the photoanode for high dye loading and fast electron transport, the search for dyes/sensitizers with strong visible light-harvesting ability, redox electrolytes for fast and efficient hole transport, and as substitutes for the electron-rich platinum (Pt) counter electrode (CE).[8–11]

The counter electrode is a key constituent which assists in collecting electrons from the external circuit passing them to the electrolyte which in turn donates these electrons to the previously oxidized dye molecules.[12] The key properties of a good CE material are; (i) high conductivity for charge transport, (ii) good electrocatalytic activity for reducing the electrolyte and (iii) excellent stability.[13] To date, Pt has been the preferred CE choice due to its metallic nature and willingness to donate electrons, however, it is susceptible to corrosion by the commonly used liquid iodide–triiodide (I^-/I_3^-) electrolyte due to the formation of PtI_4.[14,15] Variations such as different

[a]*Molecular Sciences Institute, School of Chemistry, University of the Witwatersrand, Private Bag 3, Wits, 2050, South Africa. E-mail: leratoma@mintek.co.za; Nosipho. Moloto@wits.ac.za; Tel: +27 11 709 4111; +27 11 717 6774*

[b]*Department of Chemistry, University of Limpopo, Private Bag X1106 Sovenga, 0727, South Africa*

[c]*Analytical Services Division, Mintek, 200 Malibongwe Drive, Randburg, South Africa*

carbonaceous materials, carbon–metal composites, polymers and inorganic materials such as metal chalcogenides and metal oxides have been explored as replacement CEs for platinum.[1,8,16–18] In addition to the properties listed above, a high surface area is an added advantage for a counter electrode as it allows for faster catalytic redox activity. Transition metal chalcogenides with a two-dimensional layered structure have this feature and have therefore drawn much attention as potential alternative CEs in DSSCs.[19] Some of the reported power conversion efficiencies (PCEs) when using layered materials as CEs include; 6.23% for graphene,[20] 6.6% for MoS_2 (ref. 21) and 7.01% for $MoSe_2$.[22] Another layered transition metal chalcogenide is gold selenide (AuSe), a relatively unexplored material which is electron rich and therefore has potential as a counter electrode material in DSSCs. AuSe crystallizes in monoclinic space group $C2/m$ with two polymorphs, α-AuSe and β-AuSe with lattice parameters, $a = 12.202(2)$ and $8.355(2)$ Å, $b = 3.690(7)$ and $3.663(1)$ Å and $c = 8.433(2)$ and $6.262(1)$ Å, respectively. Both crystal phases of AuSe contain Au^{1+} and Au^{3+} where the Au^{1+} is coordinated linearly to two Se atoms whilst Au^{3+} is surrounded by four Se atoms in a square planar geometry.[23,24] Herein, we report for the first time, the electrocatalytic properties of α- and β-AuSe in the redox reaction of the iodide–triiodide system.

2. Experimental section

2.1 Chemicals

Gold(III) chloride hydrate (99%), elemental selenium powder (99%), oleylamine (OLA, 70%), toluene (anhydrous, 95%), 1-methyl-2-pyrrolidinone (anhydrous NMP, 99.5%), lithium iodide (99.9%), iodine (≥99.8%), lithium perchlorate (≥95%), 4-tert-butylpyridine (98%), sodium iodide (anhydrous, ≥99.9%), acetonitrile (≥99.9%), N-719 dye (95%), white titania paste, reflector (TiO$_2$, 20.0 wt%), Whatman™ glass microfiber filter paper, fluorine doped tin oxide (FTO) coated glass slide (surface resistivity ~ 7 Ω sq^{-1}), were obtained from Sigma-Aldrich and used without any further processing. Absolute ethanol 99% was obtained from MK Chemical.

2.2 Synthesis of gold selenide

(A) For the synthesis of the predominantly α-AuSe sample, in a three-neck round bottom flask, OLA was heated to 100 °C followed by the addition of 0.28 g selenium dissolved in OLA. The temperature was further raised to 200 °C and at this point 0.17 g gold chloride dissolved in OLA was subsequently added. The reaction was carried out at 200 °C and aged for 1 h.

(B) In the synthesis of the predominantly β-AuSe sample, OLA, selenium powder and gold chloride were all placed in a three-neck flask and the temperature was raised to 200 °C over a period of 20 min. Once the required temperature was reached the reaction was aged for 1 h.

In both experiments, the mixtures were subjected to strong magnetic stirring and inert conditions during the heating as well as aging processes. Inert conditions were achieved by passing of nitrogen gas. Upon aging, ethanol was used to

flocculate the particles as well as to wash off any excess OLA. The nanomaterials were then collected by centrifugation.

2.2.1 Characterization

X-ray diffraction. A Bruker D2 phaser (D2-205530) diffractometer using secondary graphite monochromated Cu Kα radiation (λ 1.5418 Å) at 30 kV and 10 mA was used to measure the powder XRD patterns on the as-synthesized materials. Measurements were taken using a glancing angle of incidence detector at an angle of 2°, for 2θ values over 5–90° in steps of 0.036° with a step time of 0.5 s and at a temperature of 294 K.

Transmission electron microscopy. Transmission electron microscopy (TEM) was carried out on a FEI Technai T12 TEM microscope operated at an acceleration voltage of 120 kV with a beam spot size of 3 in TEM mode. The samples were initially suspended in toluene followed by placing a drop of the suspended nanomaterials on a lacey-carbon copper grid. The grid was allowed to dry at room temperature before analysis.

2.2.2 Fabrication of the dye-sensitized solar cells

Counter electrode fabrication. The counter electrode ink was prepared by dispersing 40 mg of the as-synthesized AuSe in 1 mL NMP followed by sonication for 30 min. The ink was drop-casted onto pre-cleaned FTO substrates (area ~ 1.56 cm^2) followed by baking on a hotplate at 80 °C for 10 min to allow for evaporation of the solvent and a subsequent layer was deposited and allowed to bake as previous. For reference and comparative studies, two layers of platinum were sputter-coated onto a pre-cleaned FTO substrate.

Photo-anode fabrication. The titania (TiO$_2$) paste was applied onto the conductive side of the pre-cleaned FTO substrate using the doctor blade method. The substrates were then annealed at 350 °C for 30 min to remove any residual organic compounds and to make sure the TiO$_2$ is bonded to the plate to enable better contact with the N-719 dye. The photo-sensitizing dye was made by dissolving the N-719 dye in methanol (3.0 × 10^{-4} M). A drop of the dye mixture was then added onto the annealed TiO$_2$ substrate and left overnight to dry at ambient conditions in the dark.

Device assembly. The photo-anode electrode with the sensitized TiO$_2$ side facing up was placed on the bench as the bottom plate of the cell and the counter electrode, active side facing down was placed on top of the photo-anode. The two electrodes were offset from each other and the Whatman filter paper was placed in between to act as a sponge for the redox electrolyte solution. The redox electrolyte solution was composed of 0.05 M iodine, 0.1 M lithium iodide, 0.1 M potassium iodide, 0.1 M sodium iodide and 0.5 M 4-tert-butylpyridine. The assembled device was secured with binder clips before doing the J–V measurements. The FTO used for the fabricated DSSCs of all three CEs had the same active area (~1.56 cm^2) for comparisons.

2.3 Characterization of the counter electrode (CE) thin films

Scanning electron microscopy (SEM) and energy dispersive spectroscopy (EDS) mapping were carried out on a VEGA3 TESCAN SEM microscope. The AuSe-CEs were mounted on aluminium stubs with carbon tape and analysed accordingly.

Cyclic voltammetry (CV), electrochemical impedance spectroscopy (EIS), and Tafel polarization measurements were done using Biologic: SP-300. A three-electrode system was used to conduct CV measurements at a scan rate of 100 mV s^{-1} where Ag/AgCl electrode acted as the reference electrode, Pt wire as the auxiliary electrode and the prepared AuSe-CEs acted as the working electrode. The electrolyte was made of 0.1 M LiClO$_4$, 0.001 M I$_2$ and 0.01 M LiI dissolved in anhydrous acetonitrile. The electrolyte was purged with nitrogen gas before each scan. EIS measurements were obtained using a symmetrical cell with two identical electrodes in the redox electrolyte used for DSSCs. The electrodes were analysed between 100 kHz and 100 mHz at varying open circuit potentials for each sample. The Tafel polarization measurements were conducted at a potential window of −1.0 to 1.0 V with a scan rate of 100 mV s^{-1}. The photocurrent–voltage (*J*–*V*) characteristic curves of the DSCCs were measured in ambient conditions using the HP 4141B source measure unit (SMU) under controlled illumination of 100 mW cm^{-2} (AM 1.5 G).

3. Results and discussion

Materials used in this study were previously synthesized and discussed at great length in previous publications.[23,24] X-ray diffraction was used to determine the structure of the as-synthesized powders. Fig. 1 shows the obtained diffraction patterns together with the matching standard patterns. For the two synthetic methods, mixed phased gold selenide samples were obtained with sample A having more peaks belonging to α-
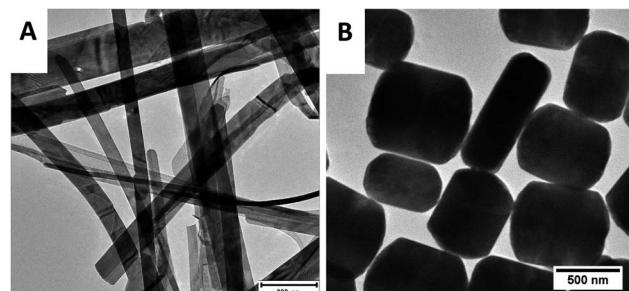

Fig. 2 TEM images of the as-obtained gold selenide materials. (A) Showing the α-AuSe nanobelts and (B) the β-AuSe nanoplates.

AuSe (PDF 00-020-0457) and sample B having more of the β-AuSe (PDF 00-020-0458) peaks. Both materials showed impurities of elemental Au (PDF 00-004-0784) and additionally sample B showed those of elemental Se (PDF 00-006-0362).

The morphology of the samples was analysed by TEM and the results are depicted in Fig. 2. Sample A revealed long belt-like structures of varying lengths and widths, on the other hand, sample B showed short plate-like structures. Owing to the sample distribution displayed on the copper grids (sample A having more belts and sample B showing more plates) it was concluded that the belts were of the α-phase while the plates were of β-phase. The mixed morphologies of the synthesized α-AuSe and β-AuSe were discussed in previous publications.[23,24]

Upon depositing the materials onto the FTO glass substrates, SEM was performed on the AuSe-CE films to confirm that no morphological changes occurred. Fig. 3(i) shows the images
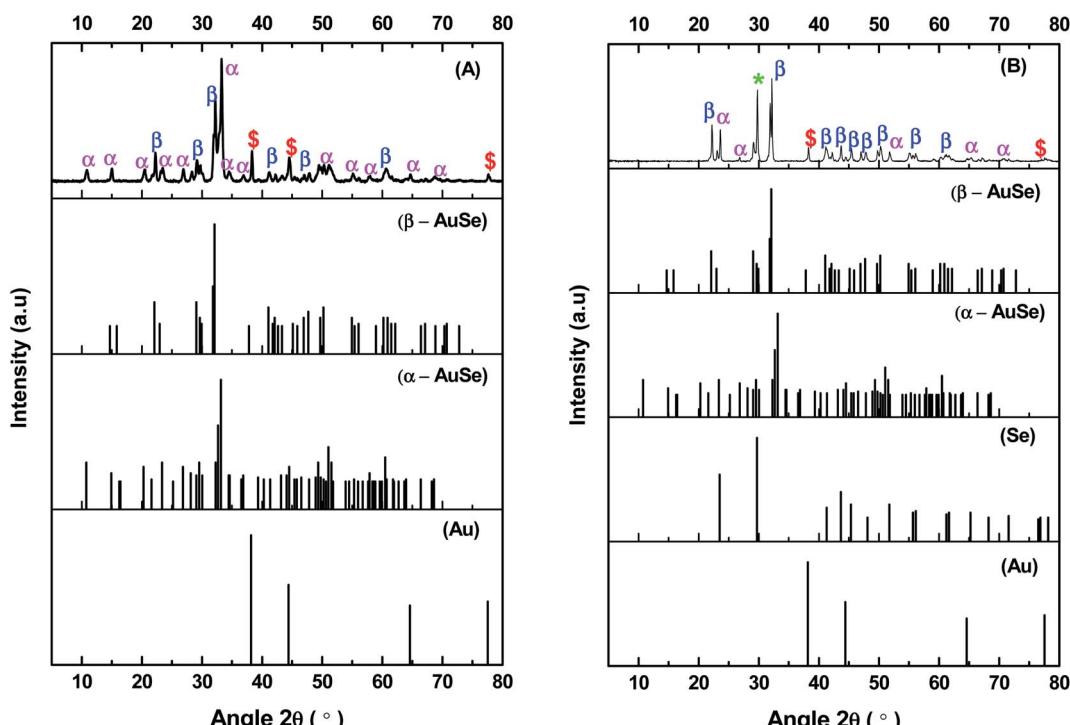

Fig. 1 Powder X-ray diffraction patterns of as-synthesized AuSe matched to standard powder patterns of α-AuSe (A), β-AuSe (B), and elemental Au & elemental Se (key: α = α-AuSe, β = β-AuSe, $ = elemental Au and * = elemental Se).
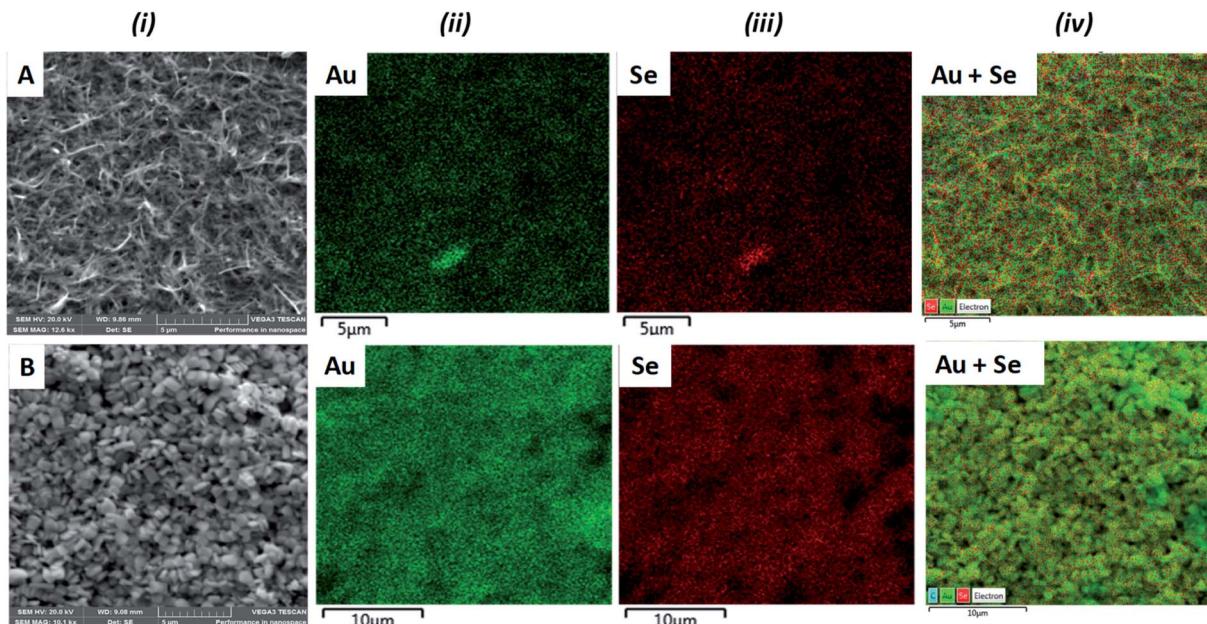
Fig. 3 (i) SEM images of (A) α-AuSe and (B) β-AuSe counter electrodes. Elemental mapping of (ii) Au, (iii) Se and (iv) summed mapping of Au and Se.

obtained during the SEM analysis where image A displays the aggregated nanobelts (α-AuSe CE) and image B shows the aggregated nanoplates (β-AuSe CE) unaltered. SEM-EDS mapping micrographs in columns (ii) and (iii) displayed even distributions of Au and Se throughout the films, respectively for both CEs. The summed mappings in column (iv) illustrates the uniformity in elemental distribution of both Au & Se giving complete homogenous AuSe-CEs.

Elemental composition was further confirmed by EDS analysis as illustrated in Fig. 4. Both CEs contained Au, Se and traces of C attributed to the capping agent. In addition, the α-AuSe-CE (Fig. 4A) also showed Sn, Si and O which comes from the FTO glass substrate used.

The electrocatalytic activity of the CEs for the I^-/I_3^- redox couple were evaluated using cyclic voltammetry (CV) at a scan rate of 100 mV s^{-1}. Fig. 5 shows CV curves of the α-AuSe and β-

AuSe CEs in comparison to that of the Pt CE. The curves of both AuSe CEs display similar duck shapes to that of Pt and therefore show compelling evidence that they can be used as alternative counter electrodes in DSSCs. The CV curves are composed of two pairs of reduction–oxidation peaks: the first pair on the left (Red_1/Ox_1) and the second pair on the right, (Red_2/Ox_2). The two pairs of redox peaks on the CV curves have similar shapes as the Pt CE suggesting that the AuSe CEs have similar catalytic activity during the redox process.[17,25] The negative (left side) and positive (right side) are represented by eqn (1) and (2), respectively.[26,27]

$$I_3^- + 2e^- \leftrightarrow 3I^- \tag{1}$$

$$3I_2 + 2e^- \leftrightarrow 3I_3^- \tag{2}$$
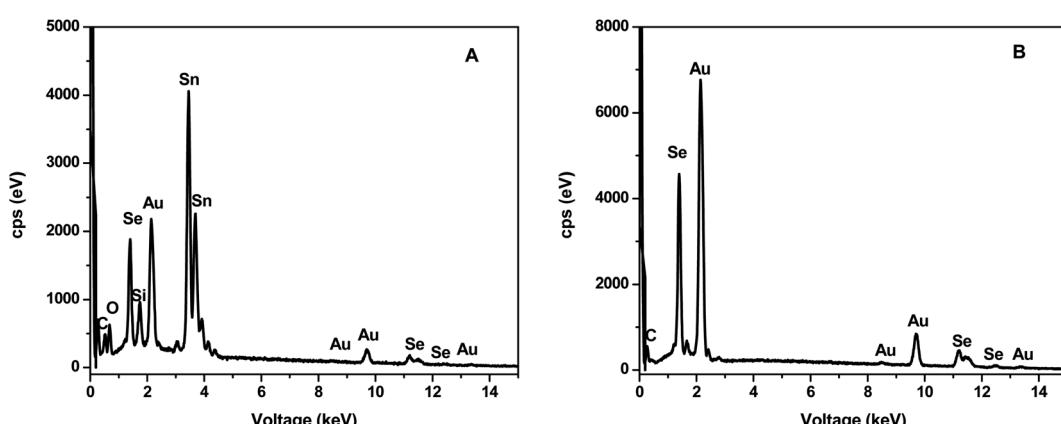
Fig. 4 SEM-EDS of (A) α-AuSe-CE and (B) β-AuSe-CE showing the elemental composition of the materials on the FTO glass substrates.
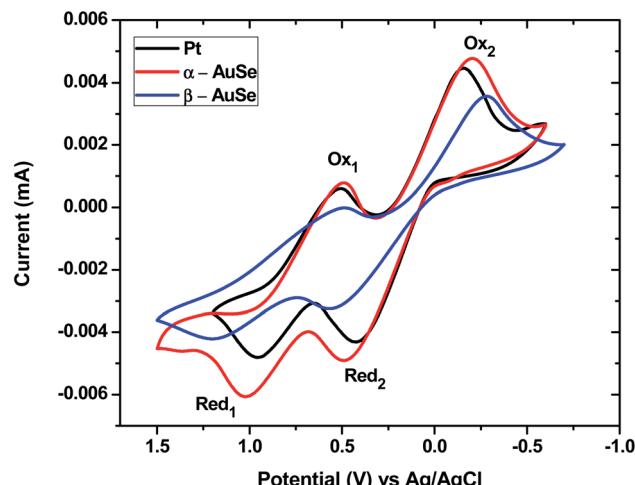
**Fig. 5** Cyclic voltammograms of the Pt, α-AuSe and β-AuSe counter electrodes at a scan rate of 100 mV s^{-1} for the I$^-$/I$_3^-$ redox couple.

Table 1 Summary of the absolute current and peak-to-peak separation (ΔE_{pp}) of each CE

CE	|Current Red$_1$ (mA)|	ΔE_{pp} (mV)
Pt	4.8	468
α-AuSe	6.1	532
β-AuSe	4.2	739

Two parameters that speak to the quality and performance of the CE are deduced from the resulting CV curves. These are the cathodic peak current density |Current Red$_1$| and the change in peak-to-peak separation (ΔE_{pp}) between Red$_1$ and Ox$_1$. A larger peak current density and smaller ΔE_{pp} indicates good electrocatalytic activity of a CE.[26,28] Table 1 compares the discussed parameters for each CE, showing α-AuSe having a higher |Current Red$_1$| of 6.1 mA than that of Pt (4.8 mA) and β-AuSe (4.2 mA). The nanobelt structure of α-AuSe gives them a much larger apparent surface area and active catalytic sites, leading to a higher current density than the Pt electrode. These findings suggest that the α-AuSe CE is the better of the two AuSe CEs. On the other hand, the α-AuSe and the β-AuSe have higher ΔE_{pp} as compared to the Pt electrode which is attributed to the higher overpotential losses in these electrodes than in the Pt electrode which can be caused by the thickness and adhesion of the electrode films thus affecting the test results.[28,29] The ΔE_{pp} values are in the order of Pt < α-AuSe < β-AuSe. Despite the larger ΔE_{pp} value for the α-AuSe, it could still serve as an alternative to the Pt electrode.

The behaviour of the CEs over different scan rate conditions was investigated and is shown in Fig. 6(a) and (b) for α-AuSe and β-AuSe, respectively. For both CEs there is an increase in |Current Red$_1$| and ΔE_{pp} with an increase in scan rate. Fig. 6(c) and (d) show the anodic and cathodic current as a function of the square root of scan rate for the two samples. The current
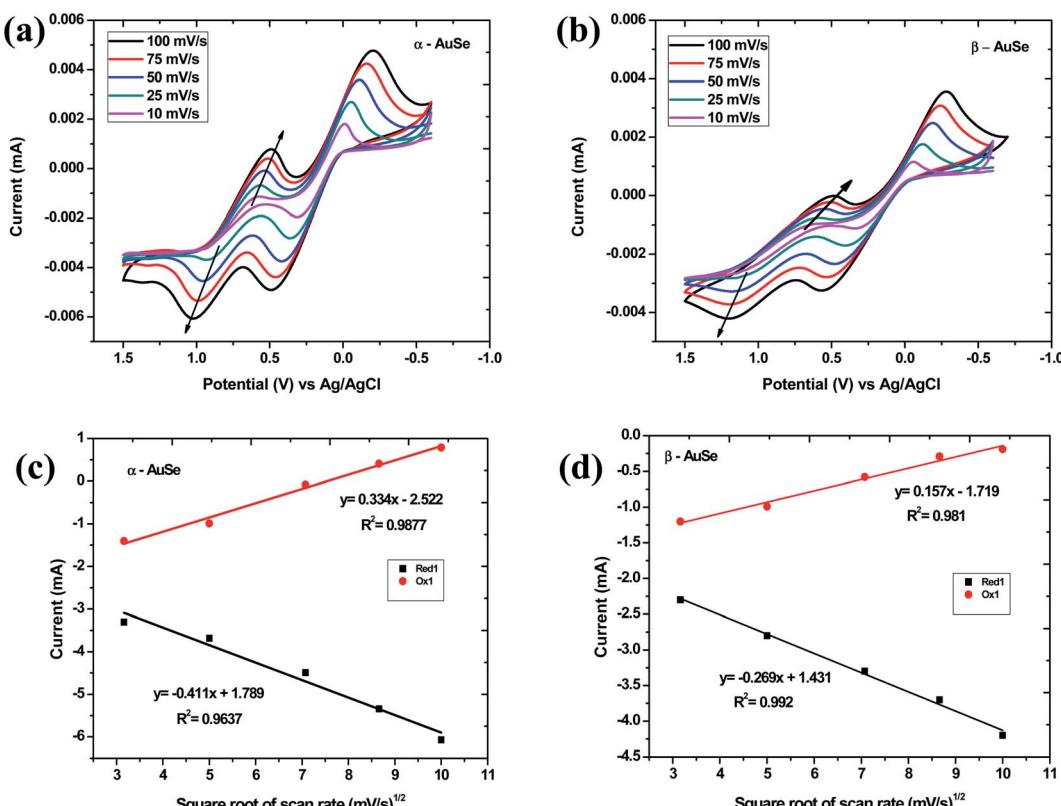

Fig. 6 Cyclic voltammograms for (a) α-AuSe and (b) β-AuSe CEs at varying scan rates from 10 mV s^{-1} to 100 mV s^{-1}. Dependence of anodic and cathodic peak currents on square root of scan rates for (c) α-AuSe and (d) β-AuSe CEs.

© 2022 The Author(s). Published by the Royal Society of Chemistry
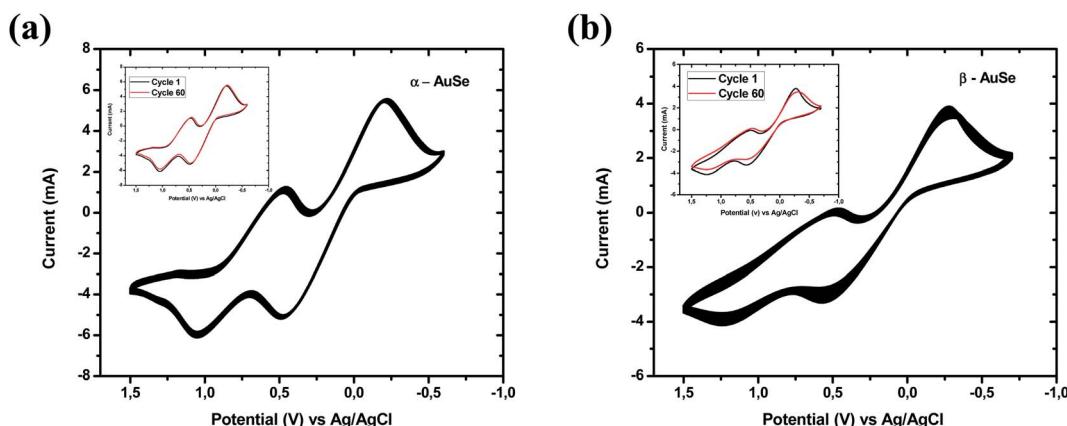
Fig. 7 Cyclic voltammograms for, (a) α-AuSe and (b) β-AuSe CEs for 60 consecutive cycles, with inserts showing the 1st and the 60th cycle for both electrodes.

density and square root of the scan rate have a relationship, according to eqn (3). As the scan rate increases, the diffusion layer becomes thinner, and the electrochemical polarization increases, resulting in a high overpotential and limited reversibility.[30] Because of the linear relationship, diffusion limits in cathodic and anodic processes may affect iodide species movement on the counter electrode surface and of evidence is the disappearance of the Red$_1$ peak at 10 mV s^{-1} suggesting this condition is not favourable for the reduction of triiodide ions using the AuSe CEs.[31,32] This linear relationship reveals that the reaction of the I$_3^-$/I$^-$ redox couple at both CEs is dominated by

ionic diffusion-controlled transport, and there is no specific interaction between the I$_3^-$/I$^-$ redox couple and the CEs.[33,34]

$$i_p = 2.69 \times 10^5 n^{3/2} A D^{1/2} V^{1/2 C} \quad (3)$$

where i_p is the peak current density, n is the number of electrons transferred, A is the area of the electrode, D is the diffusion coefficient, V is the scan rate, and C is the concentration.[30]

The stability of a counter electrode can be evaluated using successive cycle voltammetry scanning and by studying the dark current–voltage.[35–37] The reproducibility and stability of the AuSe CEs were investigated at a scan rate of 100 mV s^{-1} for 60
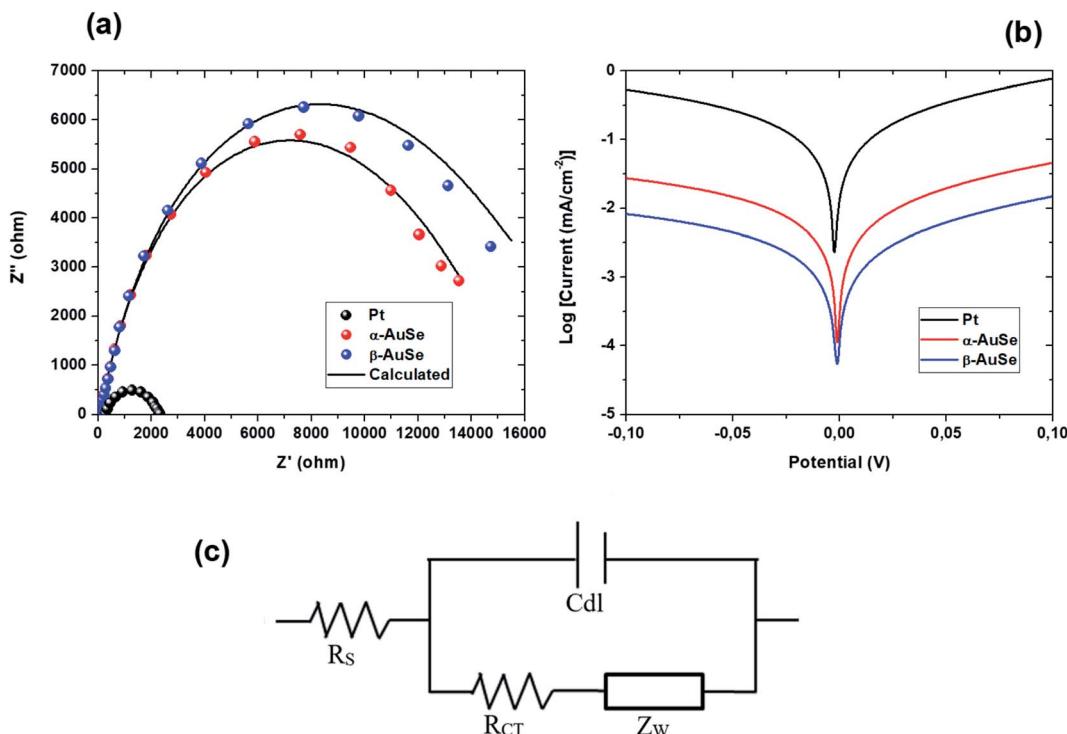

Fig. 8 (a) Nyquist plots, (b) Tafel polarization curves for the symmetric cells fabricated with Pt, α-AuSe and β-AuSe CEs and (c) the equivalent circuit.

consecutive redox cycles and the resultant curves are presented in Fig. 7(a) and (b) for α-AuSe and β-AuSe, respectively. There were minimal changes in the shapes of the CV curves. Inserts in the respective graphs show the first and sixtieth cycle and only slight changes were observed. By comparison, of the two CEs, the α-AuSe has excellent reproducibility and stability as compared to the β-AuSe, which shows some difference between the first and the sixtieth cycle with the anodic and cathodic peak current densities decreasing after the sixtieth cycle. This shows compelling evidence that the α-AuSe CE possess excellent reversible redox activity.

The electrical impedance spectroscopy (EIS) technique was used to investigate the electrocatalytic processes of the DSSCs, specifically the ability of the CEs to transfer charge to the electrolyte. For a robust counter electrode, high electrical conductivity is expected to easily facilitate electron transfers from the external circuit to reduce the I_3^- ions.[38] Fig. 8(a) shows the Nyquist plot of Pt, α-AuSe and β-AuSe which showed typically one semicircle located in the higher frequency region which can be attributed to a charge transfer resistance and (c) the

electrochemical equivalent circuit whose components show four important parameters, R_s, R_{ct}, C_{dl} and Z_w. Where the R_s is the total ohmic series resistance, R_{ct} the charge transfer resistance at an interface between the CE and the electrolyte, C_{dl} which is the double layer capacitance which denotes the charge storage capacity of the CEs and Z_w which represents the Nernst diffusion impedance in the electrolyte often employed when a line is 45° to the semi-circle at lower frequency region and explains if the interaction between the CE and the electrolyte is diffusion-controlled.[33,34] The two main parameters, R_s and R_{ct} were obtained using the Z-fit in EC-Chem software from Biologic and are listed in Table 2 for each CE. The smaller the R_s value, the higher the conductivity of the CE material and the following trend was observed Pt < α-AuSe < β-AuSe. This suggests that in terms of the two phases, the α-AuSe is the most conductive as compared to the β-AuSe. The R_s values of the AuSe electrodes are slightly higher than Pt which could be due to a lack of adhesive strength between the AuSe CE layer and the FTO glass, resulting in a larger contact resistance that decreases the conductivity of the electrode.[28] The charge transfer process represented by the R_{ct} values also suggest that the α-AuSe has better charge transfer kinetics with lower R_{ct} values as compared to the β-AuSe, represented in the order Pt < α-AuSe < β-AuSe. This can be attributed to the morphology of α-AuSe where elongated belt-like structures form charge transfer channels as compared to the less anisotropic plate-like β-AuSe.

To further investigate the catalytic activity of the CEs, Tafel polarization measurements were conducted on the symmetric cells. Fig. 8(b) shows plots of logarithmic current density ($\log J_0$)

Table 2 Electrochemical performance parameters from EIS & Tafel polarization plots for the CEs

CE	R_s (ohm)	R_{ct} (ohm)	$\log J_0$ (mA cm^{-2})	$\log J_{lim}$ (mA cm^{-2})
Pt	40.91	2587	−5.30	−3.25
α-AuSe	41.18	11 499	−5.95	−3.04
β-AuSe	41.43	14 439	−6.05	−3.37
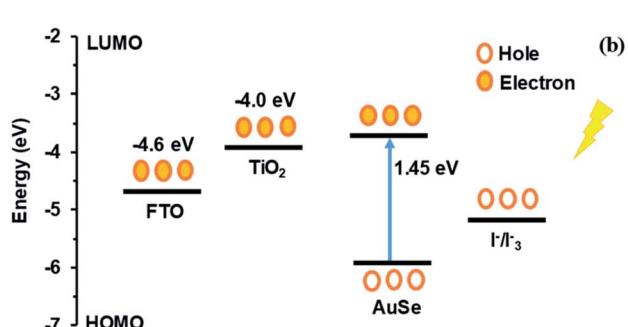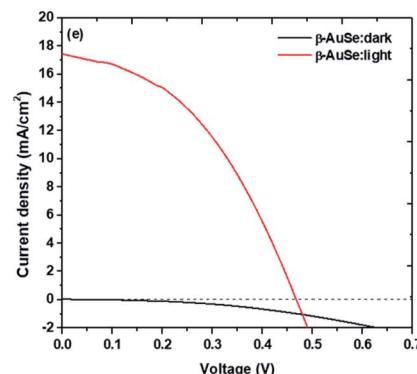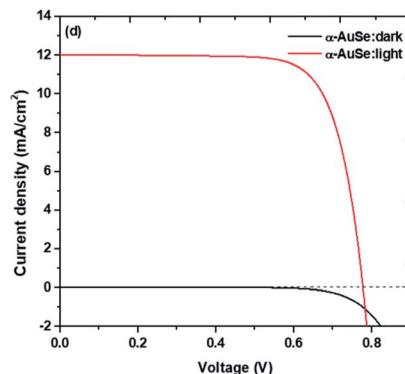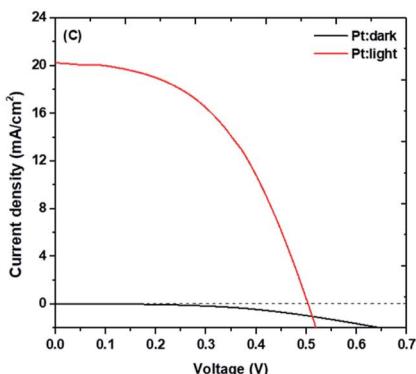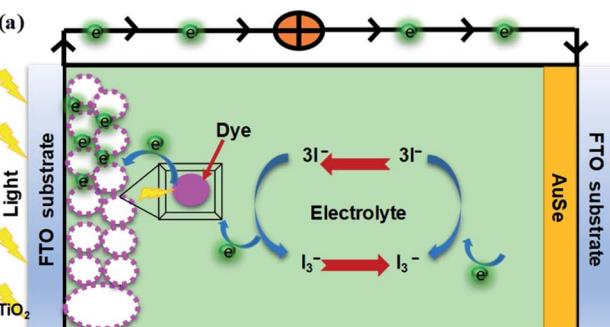
**Fig. 9** (a) Schematic of a DSSC, (b) energy diagram of the DSCC, (c) J–V curves of DSSCs with Pt, (d) α-AuSe and (e) β-AuSe CEs in the dark and under 100 mW cm^{-2} illumination.

versus potential (V) at room temperature. From the Tafel plots, we can obtain the exchange current density (J_0) and the limiting diffusion current density (J_{lim}) which are characteristic to the catalytic activity of the CEs. The parameters are influenced by both anodic or cathodic contributions of the CE and are better explained using the following equations:

$$J_0 = RT/nFR_{ct} \tag{4}$$

$$J_{lim} = 2nFDC/l \tag{5}$$

where R is the gas constant, T is the temperature (298 K), F is Faraday's constant, n ($n = 2$) is the number of electrons, R_{ct} is the charge transfer resistance, D the diffusion coefficient, C is the concentration of I_3^-, and l is the spacer thickness.[27] As can be seen from eqn (4), J_0 is inversely proportional to R_{ct}, higher J_0 values correspond to lower R_{ct} values, therefore a larger J_0 suggests better catalytic activity of the CE.[28] Likewise, from eqn (5), larger J_{lim} values indicate the larger diffusion coefficient D, which is influenced by the peak current of each CE material and indicates higher catalytic activity of the CE. From Table 2, the values of J_0 increased as per the order β-AuSe < α-AuSe < Pt. And the J_{lim} values increased in the order β-AuSe < Pt < α-AuSe. This suggests that the α-AuSe has better catalytic activity than the Pt. Overall, the results from the EIS and the Tafel plot suggests that the α-AuSe has better catalytic activity as compared to the β-AuSe, which is consistent with the CV data.

Fig. 9 shows the photocurrent density–voltage (J–V) curves of the DSSCs assembled from the Pt and AuSe CEs, both in dark and upon illumination. The dark current for the three devices did not show much difference hence signifying relatively good stability similar to what is observed in the successive CV scans. The respective parameters including the open circuit voltage (V_{oc}), short circuit current density (J_{sc}), fill factor (FF) and power conversion efficiency (PCE) are summarized in Table 3.

From the results shown in Table 3, of the AuSe phases, it can be observed that the α-AuSe has the highest efficiency of 6.94% as compared to the β-AuSe, which has an efficiency of 3.47%, however α-AuSe has a higher efficiency than Pt due to a better V_{oc}. The V_{oc} usually increases with an increasing bandgap, α-AuSe has been shown to have a bandgap of 1.45 eV while the β-AuSe bandgap is narrower.[27,39] Notably, the α-AuSe has the highest FF. A high voltage generally results in a high FF. The low FF values are due to the high R_s values and low shunt resistance (R_{sh}) values which are caused by increasing recombination at interfaces of the DSSCs.[40] The lower efficiency of the Pt CE is due to recombination as indicated by the low V_{oc} and FF; this can be attributed to the roughness of the thin film which creates recombination sites.[41] The PCEs of the α-AuSe CE is comparable to some of the reported PCEs of different layered materials as

Table 3 J–V parameters of DSSCs with Pt and AuSe CEs

| Counter electrode	J_{sc} (mA cm^2)	V_{oc} (V)	FF (%)	PCE (%)
Pt	20.26 ± 0.08	0.52 ± 0.02	46 ± 0.2	4.89 ± 0.23
α-AuSe	12.00 ± 0.03	0.79 ± 0.01	73 ± 0.4	6.94 ± 0.09
β-AuSe	17.43 ± 0.10	0.49 ± 0.02	41 ± 1.0	3.47 ± 0.18
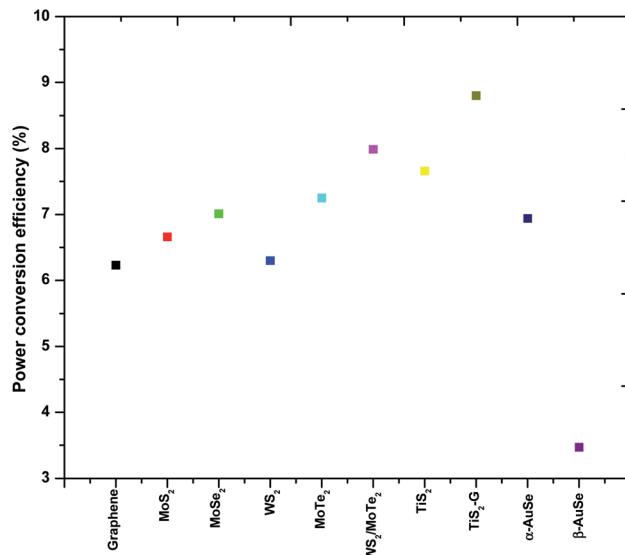
Fig. 10 A comparison plot showing the trend in power conversion efficiencies (PCEs) of a few 2-dimensional layered transition metal chalcogenides.

CEs. Examples include; 6.23% for graphene,[20] 6.6% for MoS$_2$,[21] 7.01% for MoSe$_2$,[22] 6.30% for WS$_2$,[42] 7.25% for MoTe$_2$,[43] 7.99% for WS$_2$/MoTe$_2$,[44] 7.66% for TiS$_2$ and 8.80% for TiS$_2$ nanosheets assembled and decorated on graphene (TiS$_2$–G)[16] as shown in Fig. 10. The lower values are attributed to the lower FF. This could be due to the presence of the mixed phases of AuSe as observed in the XRD. Nevertheless, the J_{sc} are comparable.

4. Conclusion

In summary, colloidal gold selenide was successfully synthesized and the as synthesized materials were effectively incorporated onto FTO glass to form homogenized counter electrode films. Powder XRD showed biphasic materials where both α and β-AuSe phases present in each sample, however, a level of dominance was observed in each. TEM depicted long belt-like structures for the α-AuSe dominated sample and short plate-like structures for the β-AuSe dominated sample. SEM analysis confirmed the morphology of the nanostructures on the CE films, it further validated the elemental composition with EDS mapping. Cyclic voltammetry showed compelling evidence that both α-AuSe and β-AuSe have potential use in dye sensitized solar cells as counter electrodes with good electrocatalytic activity towards reduction of I_3^- ions in the iodide–triiodide redox couple. The higher cathodic peak current (|Current Red$_1$|) of 6.1 mA and lower ΔE_{pp} value of 532 mV for the α-AuSe CE, makes it the more preferred of the two CEs, compared to 4.2 mA and 739 mV for the β-AuSe CE. The two AuSe CEs gave larger ΔE_{pp} values than the Pt CE (468 mV). The EIS and Tafel plot data followed the same trend hence indicating the catalytic activities of β-AuSe < α-AuSe < Pt. The results from complete DSSCs were extracted from the J–V curves, α-AuSe had the highest PCE (6.94%) as compared to Pt (4.89%) and β-AuSe (3.47%). The lower efficiency for Pt was attributed to the fabrication process.

Conflicts of interest

There are no conflicts to declare.

Acknowledgements

References

1 S. Yun, Y. Liu, T. Zhang and S. Ahmad, *Nanoscale*, 2015, **7**, 11877–11893.

2 S. P. Mohanty, V. More and P. Bhargava, *RSC Adv.*, 2015, **5**, 18647–18654.

3 K. Kakiage, Y. Aoyama, T. Yano, K. Oya, J. I. Fujisawa and M. Hanaya, *Chem. Commun.*, 2015, **51**, 15894–15897.

4 B. O'Regan and M. Gratzel, *Nature*, 1991, **353**, 737–740.

5 S. Yun, Y. Qin, A. R. Uhl, N. Vlachopoulos, M. Yin, D. Li, X. Han and A. Hagfeldt, *Energy Environ. Sci.*, 2018, **11**, 476–526.

6 M. Kokkonen, P. Talebi, J. Zhou, S. Asgari, S. A. Soomro, F. Elsehrawy, J. Halme, S. Ahmad, A. Hagfeldt and S. G. Hashmi, *J. Mater. Chem. A*, 2021, **9**, 10527–10545.

7 S. Yun, A. Hagfeldt and T. Ma, *Adv. Mater.*, 2014, **26**, 6210–6237.

8 M. Ye, X. Wen, M. Wang, J. Iocozzia, N. Zhang, C. Lin and Z. Lin, *Mater. Today*, 2015, **18**, 155–162.

9 J. Wu, Z. Lan, J. Lin, M. Huang, Y. Huang, L. Fan and G. Luo, *Chem. Rev.*, 2015, **115**, 2136–2173.

10 M. R. Narayan, *Renewable Sustainable Energy Rev.*, 2012, **16**, 208–215.

11 S. Thomas, T. G. Deepak, G. S. Anjusree, T. A. Arun, S. V. Nair and A. S. Nair, *J. Mater. Chem. A*, 2014, **2**, 4474–4490.

12 D. Nechiyil, B. P. Vinayan and S. Ramaprabhu, *J. Colloid Interface Sci.*, 2017, **488**, 309–316.

13 Y. S. Yen, H. H. Chou, Y. C. Chen, C. Y. Hsu and J. T. Lin, *J. Mater. Chem.*, 2012, **22**, 8734–8747.

14 S. S. Nemala, P. Kartikay, R. K. Agrawal, P. Bhargava, S. Mallick and S. Bohm, *Sol. Energy*, 2018, **169**, 67–74.

15 E. Olsen, G. Hagen and S. E. Lindquist, *Sol. Energy Mater. Sol. Cells*, 2000, **63**, 267–273.

16 X. Meng, C. Yu, B. Lu, J. Yang and J. Qiu, *Nano Energy*, 2016, **22**, 59–69.

17 X. Li, J. Bai, B. Zhou, X. Yuan, X. Zhang and L. Liu, *Chem.–Eur. J.*, 2018, **24**, 11444–11450.

18 U. Ahmed, M. Alizadeh, N. A. Rahim, S. Shahabuddin, M. S. Ahmed and A. K. Pandey, *Sol. Energy*, 2018, **174**, 1097–1125.

19 E. Singh, K. S. Kim, G. Y. Yeom and H. S. Nalwa, *RSC Adv.*, 2017, **7**, 28234–28290.

20 S. S. Nemala, P. Kartikay, S. Prathapani, H. L. M. Bohm, P. Bhargava, S. Bohm and S. Mallick, *J. Colloid Interface Sci.*, 2017, **499**, 9–16.

21 S. Vijaya, G. Landi, J. J. Wu and S. Anandan, *Electrochim. Acta*, 2019, **294**, 134–141.

22 X. Yuan, B. Zhou, X. Zhang, Y. Li and L. Liu, *Electrochim. Acta*, 2018, **283**, 1163–1169.

23 L. F. E. Machogo, P. Tetyana, R. Sithole, S. S. Gqoba, N. Phao, M. Airo, P. M. Shumbula, M. J. Moloto and N. Moloto, *Appl. Surf. Sci.*, 2018, **456**, 973–979.

24 L. F. E. Machogo, M. Mthimunye, R. K. Sithole, P. Tetyana, N. Phao, G. N. Ngubeni, M. Mlambo, P. S. Mduli, P. M. Shumbula and N. Moloto, *New J. Chem.*, 2019, **43**, 5773–5782.

25 X. Wu, J. Duan, Y. Zhao, X. Yang, H. Chen, B. He and Q. Tang, *Sol. Energy*, 2019, **180**, 85–91.

26 J. Wu, Q. Li, L. Fan, Z. Lan, P. Li, J. Lin and S. Hao, *J. Power Sources*, 2008, **181**, 172–176.

27 X. Qian, H. Li, L. Shao, X. Jiang and L. Hou, *ACS Appl. Mater. Interfaces*, 2016, **8**, 29486–29495.

28 Y. Liu, S. Yun, X. Zhou, Y. Hou, T. Zhang, J. Li and A. Hagfeldt, *Electrochim. Acta*, 2017, **242**, 390–399.

29 S. Yun, J. Shi, M. Si, M. Sun, Y. Zhang, A. Arshad and C. Yang, *J. Colloid Interface Sci.*, 2021, **601**, 12–29.

30 M. Wu, Y. Wang, X. Lin, N. Yu, L. Wang, L. Wang, A. Hagfeldt and T. Ma, *Phys. Chem. Chem. Phys.*, 2011, **13**, 19298–19301.

31 S. Biallozor and A. Kupniewska, *Electrochem. Commun.*, 2000, **2**, 480–486.

32 M. Ikegami, K. Miyoshi and T. Miyasaka, *Appl. Phys. Lett.*, 2007, **90**, 153122.

33 G. Yue, W. Wu, X. Liu and H. Zheng, *Sol. Energy*, 2018, **167**, 137–146.

34 T. Zhang, S. Yun, X. Li, X. Huang, Y. Hou, Y. Liu and J. Li, *J. Power Sources*, 2017, **340**, 325–336.

35 C. Wang, S. Yun, Q. Fan, Z. Wang, Y. Zhang, F. Han, Y. Si and A. Hagfeldt, *J. Mater. Chem. A*, 2019, **7**, 14864–14875.

36 S. Yun, H. Pu, J. Chen, A. Hagfeldt and T. Ma, *ChemSusChem*, 2014, **7**, 442–450.

37 S. Yun, A. Hagfeldt and T. Ma, *ChemCatChem*, 2014, **6**, 1584–1588.

38 Q. S. Jiang, R. Chen, X. Guo, Y. Zhu, W. Cheng, W. Li, X. Yang and H. C. Chen, *Sol. Energy*, 2019, **179**, 59–66.

39 C. Tang, L. Zhang, C. Zhang, J. Macleod, K. Ostrikov and A. Du, *Nanoscale Horiz.*, 2020, **5**, 366–371.

40 T. Kolokoto, V. Mashindi, L. F. E. Machogo-phao, Z. B. Ndala, N. P. Shumbula, S. S. Nkabinde, G. N. Ngubeni, S. S. Gqoba, K. P. Mubiayi and N. Moloto, *RSC Adv.*, 2021, **11**, 31159–31173.

41 Z. Huang, G. Natu, Z. Ji, M. He, M. Yu and Y. Wu, *J. Phys. Chem.*, 2012, **116**, 26239–26246.

42 S. Hussain, S. Shaikh, D. Vikraman, R. S. Mane, O. S. Joo, M. Naushad and J. Jung, *RSC Adv.*, 2015, **5**, 103567–103572.

43 S. Hussain, S. A. Patil, D. Vikraman and N. Mengal, *Sci. Rep.*, 2018, **6**, 4–11.

44 S. Hussain, S. A. Patil, A. A. Memon, D. Vikraman, H. G. Abbas, S. H. Jeong, H. S. Kim, H. S. Kim and J. Jung, *Inorg. Chem. Front.*, 2018, **5**, 3178–3183.